Yield Estimation and Event Discrimination of the 4 August 2020 Beirut Chemical Explosion

Lei Zhang[1,2], Lian-Feng Zhao*[1,3], Xiao-Bi Xie[4], Xi He[1], and Zhen-Xing Yao[1]

Abstract

We investigate the 4 August 2020 Beirut accidental chemical explosion based on regional seismic data recorded at both on- and off-shore stations. The *Lg*-wave body-wave magnitude is $m_b(Lg) = 3.30 \pm 0.46$ for the Beirut explosion. The explosive yield obtained using an empirical magnitude-yield relation based on a fully buried explosion source model is only 0.112 kt. Alternatively, the yield estimated using an empirical relation between the yield and crater size is 1.22 kt, with the uncertainties between 0.48 and 2.3 kt. The latter is closer to reality. The *P/S* spectral amplitude ratios, including *Pg*/*Lg*, *Pn*/*Lg*, and *Pn*/*Sn*, are calculated for the Beirut explosion and nearby natural earthquakes. We find the *P/S* spectral ratios are effective in discriminating the explosion from earthquakes in the Northwestern Arabia plate. By comparing the spectral ratios of large open-pit explosions, including the Beirut, Xiangshui, and Tianjin explosions, with those from historical nuclear explosions, buried small chemical explosions, and natural earthquakes, we further investigate the detailed differences of network-averaged *P/S* spectral ratios between different source types.

Cite this article as Zhang, L., L.-F. Zhao, X.-B. Xie, X. He, and Z.-X. Yao (2022). Yield Estimation and Event Discrimination of the 4 August 2020 Beirut Chemical Explosion, *Seismol. Res. Lett.* **XX**, 1–11, doi: 10.1785/0220210363.

Supplemental Material

Introduction

On 4 August 2020, a massive explosion occurred in the city of Beirut, Lebanon. This accident was preliminarily reported to be caused by the deflagration of 2750 metric tons of ammonium nitrate stocked at the port district of Beirut (Guglielmi, 2020). The serious explosion caused at least 200 fatalities and about 6500 injuries (Nemer, 2021). The U.S. Geological Survey (USGS) reported the local magnitude of this event to be M_L 3.3, with an origin time of 15:08:18 in universal time (UTC), a focal depth of 0 km, and an epicenter of 33.901° N and 35.519° E.

Since the 1980s, the Comprehensive Nuclear Test Ban Treaty requires monitoring underground nuclear explosions with their yields ≤1 kt or magnitudes ≤4. Following this, a series of seismic methods were developed to (1) determine the event location (Wagner *et al.*, 2013; Zhang and Wen, 2013; Zhao, Xie, *et al.*, 2016; Gibbons *et al.*, 2017; Myers *et al.*, 2018; Pasyanos and Myers, 2018; Schaff *et al.*, 2018; He *et al.*, 2021; Yang *et al.*, 2021); (2) calculate the seismic magnitude and estimate the yield (e.g., Nuttli, 1973, 1986b; Bennett and Murphy, 1986; Ringdal *et al.*, 1992; Bowers *et al.*, 2001; Murphy *et al.*, 2013; Zhang and Wen, 2013; Zhao, Xie, *et al.*, 2016; Pasyanos and Myers, 2018); and (3) discriminate the explosions from natural earthquakes (Kim and Richards, 2007; Shin *et al.*, 2010; Zhao, Xie, *et al.*, 2016; Zhao *et al.*, 2017; Walter *et al.*, 2018; Koper *et al.*, 2020; Ma *et al.*, 2021). The Beirut explosion attracted wide attention and there were many studies since its occurrence. Ghalib *et al.* (2021) used the Bayesian methodology and regional seismic dataset to locate the epicenter and corrected the origin time to 1.05 s later than the USGS origin time. Rigby *et al.* (2020) best estimated the yield to be 0.5 kt by analyzing the blast velocity in 16 live videos. Jorge (2021) estimated the yield to be 1.0 kt based on the fireball expansion speed. Pilger *et al.* (2021) estimated a yield of 1.1 kt by matching the observed and estimated damages versus the distance from the center of the explosion.

In this article, we aim to investigate the source characteristics of the Beirut explosion including the magnitude calculation, yield estimation, and discrimination with natural earthquakes. There are two commonly used methods to discriminate between explosions and earthquakes, that is, the $m_b - M_s$ empirical relations and the regional *P/S* spectral ratio method. The former is

1. Key Laboratory of Earth and Planetary Physics, Institute of Geology and Geophysics, Chinese Academy of Sciences, Beijing, China, https://orcid.org/0000-0001-5475-7429 (LZ); https://orcid.org/0000-0002-1400-3064 (L-FZ); https://orcid.org/0000-0002-4029-1266 (Z-XY); 2. University of Chinese Academy of Sciences, Beijing, China; 3. Heilongjiang Mohe Observatory of Geophysics, Institute of Geology and Geophysics, Chinese Academy of Sciences, Beijing, China; 4. Institute of Geophysics and Planetary Physics, University of California at Santa Cruz, Santa Cruz, California, U.S.A.

*Corresponding author: zhaolf@mail.iggcas.ac.cn

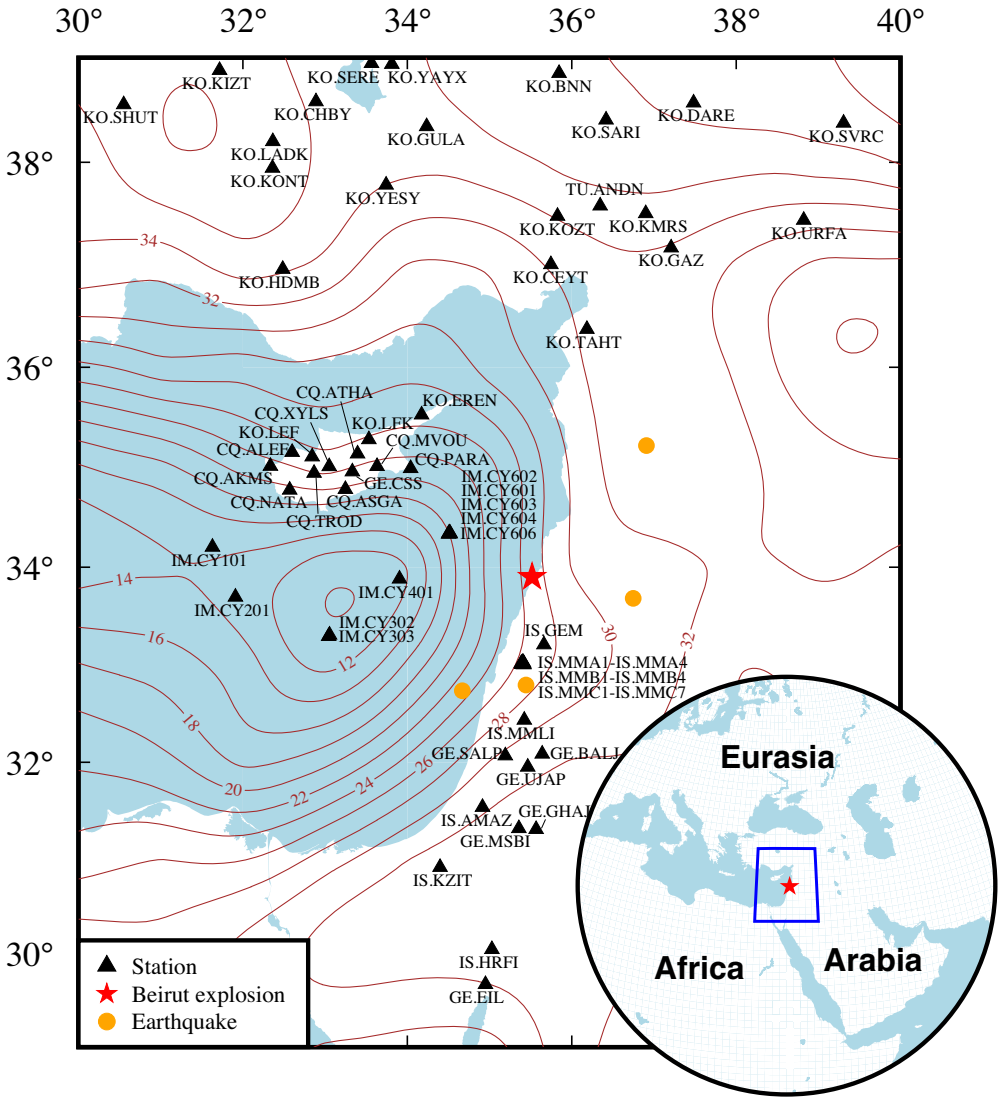

Figure 1. Map showing the crustal isopach (thin brown lines) in the study area, overlapped with locations of the Beirut explosion (solid red star), four nearby earthquakes (solid orange circles), and stations (solid black triangles). The inset coastline map on the right bottom corner shows the locations of the study area (blue trapezoid) and the Beirut explosion (solid red star). The color version of this figure is available only in the electronic edition.

Regional Dataset

In this study, we collected broadband digital seismic data from the Beirut explosion and four nearby natural earthquakes that occurred between July 2018 and August 2020 from both onshore and offshore stations for the yield estimation and the discrimination between the explosion and natural earthquakes. The dataset includes 221 vertical-component seismograms recorded by 76 broadband digital stations from the National Observatory of Athens Seismic Network, GEOFOrschungsNetz, International Miscellaneous stations, Bogazici University Kandilli Observatory and Earthquake Research Institute, Israel National Seismic Network, and Cyprus Broadband Seismological Network. Figure 1 illustrates the locations of stations and events, overlaid with crust isopaches based on the CRUST1.0 model (Laske *et al.*, 2013). Source parameters of all events are listed in Table 1 and the station parameters are listed in Table S1, available in the supplemental material to this article.

The Beirut chemical explosion generated abundant local and regional seismic phases. As this region is composed of continental, continental shelf, and oceanic structures, the features of seismograms from this explosion vary between different types of stations (Fig. 2). The seismograms recorded by ocean-bottom stations are characterized by strong *T* phases and weaker *P* and *Lg* waves. The observations from stations at the eastern Cyprus island are characterized by strong *T* phases, whereas those recorded at the western island lack *T* phases, and the weak *P* and *Lg* waves with a low signal-to-noise ratio (SNR) can be observed. The seismograms recorded from stations located on the Arabia plate and Anatolian plateau lack *T* phases but are dominated by *P* waves at local distances, and *Lg* waves at regional distances. The *T* phase is a seismic wave converted from the acoustic wave traveling through the low-velocity SOund Fixing And Ranging channel in the oceanic water column

very effective for large events using globally recorded teleseismic data but cannot provide satisfactory discrimination for low yield events over regional distances (Stevens and Day, 1985; Fisk *et al.*, 2002; Bonner *et al.*, 2008; Chun *et al.*, 2011; Selby *et al.*, 2012; Murphy *et al.*, 2013; Ma *et al.*, 2021). On the other hand, the regional *P/S* (*Pg/Lg*, *Pn/Lg*, *Pn/Sn*) spectral ratio method can successfully separate explosions from earthquakes at regional distances (e.g., Taylor *et al.*, 1989; Kim *et al.*, 1993; Walter *et al.*, 1995, 2007; Xie, 2002; Fisk, 2007; Richards and Kim, 2007; Allmann *et al.*, 2008; Zhao, Xie, *et al.*, 2016; He *et al.*, 2018; Pyle and Walter, 2019; Ma *et al.*, 2021; Song *et al.*, 2021). The Beirut chemical explosion provides a new dataset to check the applicability of the regional *P/S* spectral ratio method in the northwestern Arabia plate.

TABLE 1
Event Parameters Used in This Study

Event		Origin Time (UTC) yyyy/mm/dd hh:mm:ss.ss	Latitude (°N)	Longitude (°E)	Depth (km)		Magnitude		
						$m_b(P)$	$m_b(Lg)$	σ	N
Beirut explosion	BEx	2020/08/04 15:08:19.05	33.901	35.519	0.0	M_L 3.3	3.30	0.46	23
Natural earthquake	NEq1	2020/11/30 13:47:05.11	35.223	36.909	13.6	4.4	4.32	0.56	54
	NEq2	2020/11/26 22:08:26.00	33.684	36.748	10.0	4.1	4.52	0.43	42
	NEq3	2020/02/06 04:53:51.70	32.739	34.670	10.0	4.0	4.22	0.43	15
	NEq4	2018/07/04 19:45:40.04	32.797	35.444	10.0	4.7	4.78	0.42	31

(Talandier and Okal, 1998; Buehler and Shearer, 2015). For seismograms recorded by ocean-bottom stations through the pure oceanic path, the apparent velocity of the *T* phase is close to 1.55 km/s. For coastal stations, the apparent velocity varies depending on the fractional lengths of the oceanic and continental portions of the path. The *T* phase attenuates faster when encountering the island structure and converting to the conventional body waves (Koyanagi *et al.*, 1995; Talandier and Okal, 1998). The *Lg* wave is usually understood as the sum of supercritically reflected *S* waves trapped in the crustal waveguide (Xie and Lay, 1994). Previous studies found that oceanic-to-continental crust transitions can significantly attenuate or even block the *Lg* wave propagation (Zhang and Lay, 1995). The observed *Lg* waves at stations CQ.AKMS, CQ.NATA, CQ.ALEF, and GE.CSS indicate that the approximately 22-km thick island crust can properly carry the *Lg*-wave propagation. We further compared the vertical-component seismograms recorded at station GE.EIL for the Beirut explosion and three nearby natural earthquakes in Figure 3. The explosion waveform shows the clear impulsive *P*-wave onset and relatively weak *S*-type waves, whereas the waveforms from the nearby earthquakes show opposite characteristics. This is typical as the explosions mainly radiate a large amount of compressional energy while the natural earthquakes are caused by dislocation sources that generate strong *S* waves.

Event Magnitude and Yield Estimation

The *Lg* wave provides us a useful signal to calculate the body-wave magnitude for small earthquakes and explosions with only a few regional stations (Nuttli, 1986b). Here, following Zhao *et al.* (2008, 2012), we used both the third peak (TP) (Nuttli, 1973, 1986a) and the root mean square (rms) amplitudes (Patton and Schlittenhardt, 2005) to calculate the magnitudes. The origin time was corrected based on Ghalib *et al.* (2021) and the attenuation factor was given by integrating the *Q* along the great circle ray path based on the broadband *Lg*-wave attenuation model in the Middle East (Zhao and Xie, 2016) rather than using a regional average *Q*. To improve the accuracy of the magnitude measurements, only continental stations are used to calcultate the $m_b(Lg, \mathrm{TP})$ and $m_b(Lg, \mathrm{rms})$ of the Beirut explosion and four nearby earthquakes, and the results are used to calculate station corrections. Then, after correcting with station terms, we calculate the network-averaged values by adding both the $m_b(Lg, \mathrm{TP})$ and $m_b(Lg, \mathrm{rms})$ measurements together. The obtained magnitude for the Beirut explosion was $m_b(Lg) = 3.30 \pm 0.46$. To compare with the USGS result, we converted the local magnitude M_L 3.3 by USGS to body-wave magnitude m_b using the relationship $0.77m_b - 0.64M_L = 0.73$ (Ambraseys, 1990). The resulting m_b was 3.69, about 0.39 magnitude units larger than our $m_b(Lg)$. By adopting an empirical magnitude-yield relation for a fully buried source in Novaya Zemlya, the continental shelf of the European Arctic region (Bowers *et al.*, 2001) and $m_b(Lg) = 3.30 \pm 0.46$, the estimated yield was 0.112 (0.046 ~ 0.275) kt, which greatly underestimated the yield, indicating a fully buried equation is inappropriate for an open-pit explosion.

Alternatively, we turned to another empirical equation for above-the-ground explosions obtained by Ambrosini *et al.* (2002) through small chemical explosion experiments. The yield can be estimated by fitting the observed crater diameter *D* and the height of the burst *d* (both in meter) to the equation:

$$\log\left(\frac{\frac{D}{2}}{d}\right) = 1.241 \log\left(\frac{Y^{\frac{1}{3}}}{d}\right) - 0.818, \quad (1)$$

in which Y is the explosion yield in kg of trinitrotoluene (TNT). The chemical charge of experiments supporting this equation was between 1 and 10 kg, and the height of the burst ranges from 0 to 1 m. We assumed that equation (1) is valid for the Beirut explosion, for which the explosives were stored in a cuboid-shaped warehouse. Based on the satellite photo (Fig. 4b), the Beirut explosion left an 80 m by 120 m elliptical crater. We used the average of the major and minor axes, approximately 100 m, as the diameter of the crater *D*. The height of the burst is assumed to range from 0.2 to 3.0 m,

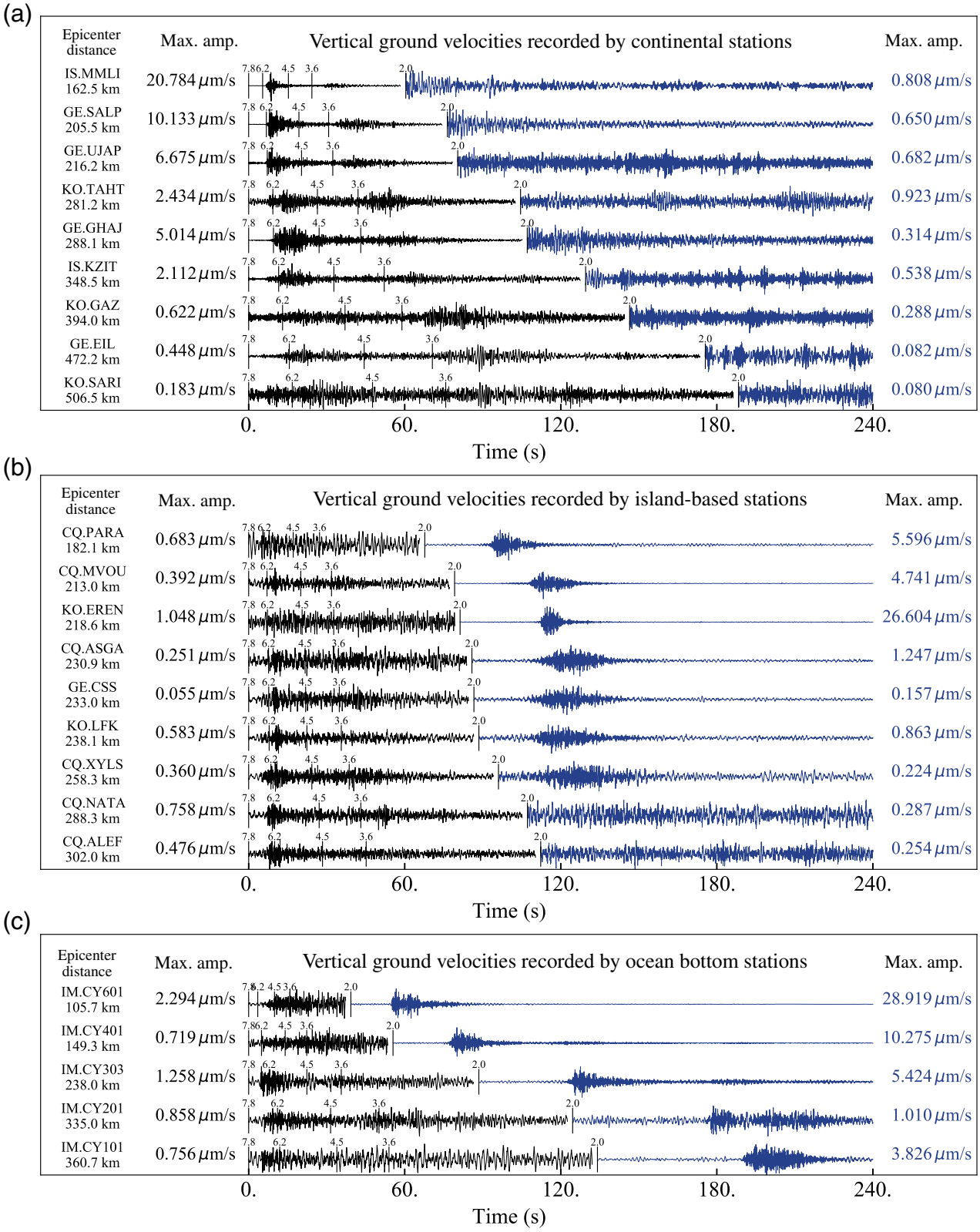

Figure 2. Vertical-component velocity seismograms bandpass filtered between 0.5 and 10.0 Hz for the 4 August 2020 Beirut explosion. Seismograms were recorded by (a) continental stations, (b) island-based stations, and (c) ocean-bottom stations. Because of the large amplitude contrast between seismic body waves and the *T* phase, seismograms are divided into two sections at group velocity 2.0 km/s and normalized separately. The station names, epicentral distances, and maximum amplitudes for the first section are listed on the left, and the maximum amplitudes for the second section are listed on the right. Marked on the waveforms are group velocities. The color version of this figure is available only in the electronic edition.

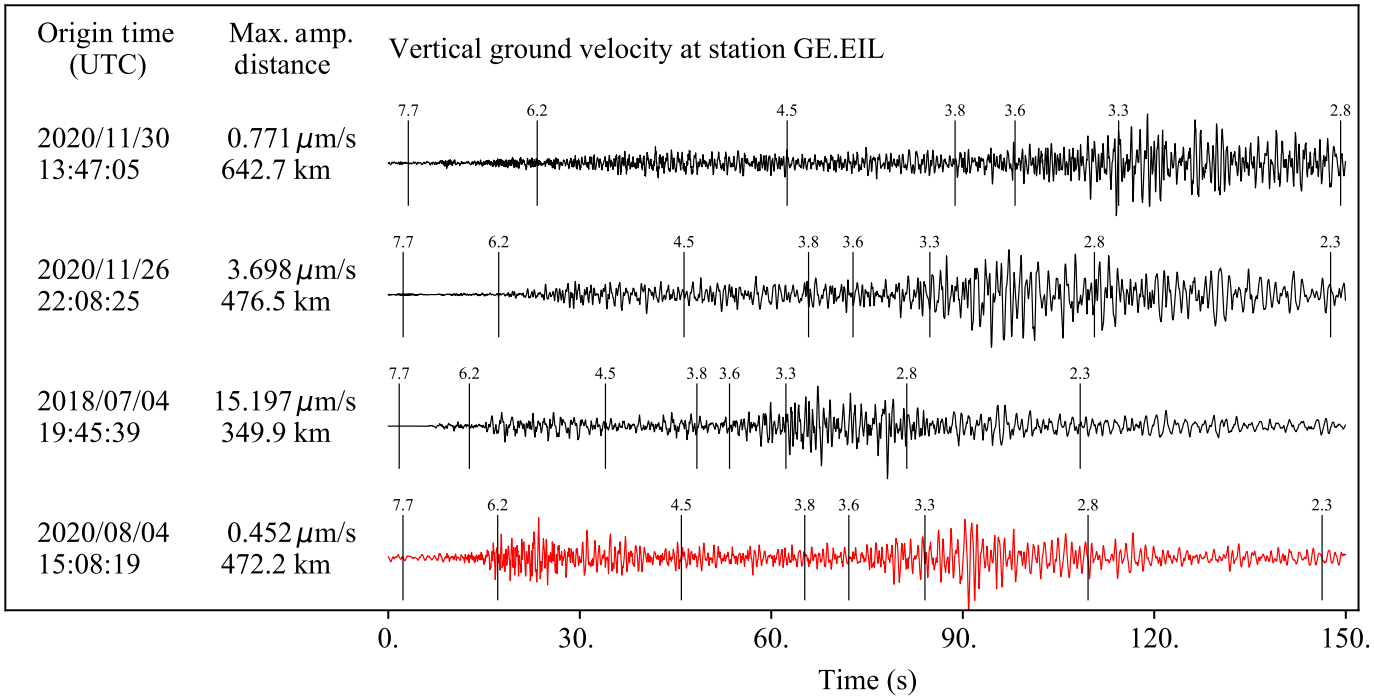

Figure 3. Normalized vertical component velocity seismograms recorded at station GE.EIL. The waveforms are bandpass filtered between 0.5 and 10.0 Hz. The top three traces are from three natural earthquakes and the bottom trace is from the Beirut explosion. Their origin times, maximum amplitudes, and epicentral distances are listed on the left. Marked on the waveforms are group velocities. Note the relatively strong *P* waves for the explosion source. The color version of this figure is available only in the electronic edition.

and the yield is estimated to be from 0.48 to 2.3 kt. The lower limit is estimated from the condition that the warehouse was covered with 2.75 kt ammonium nitrate (Guglielmi, 2020). The size of the warehouse can be estimated from the rectangle which was on the east of the crater and left by the nearby warehouse (Fig. 4b). It was approximately 100 m by 40 m, and the density of the ammonium nitrate is 1.72×10^3 kg/m^3. Therefore, the explosives would be 0.4 m high, which generated a height of the burst of 0.2 m. Alternatively, the upper limit, 3.0 m, is from half of the general height of the warehouse, 6 m. Considering the storage efficiency and the photo of the warehouse before the explosion from the Internet (Fig. S2), we assumed that the most acceptable height of the burst is 1.0 m. Therefore, the acceptable yield estimation for the Beirut explosion based on the extended empirical crater size-yield relation of Ambrosini *et al.* (2002) was 1.22 kt. Table 2 compares the yield estimations from different studies, and they were mostly around 1.0 kt, very close to the estimated yield. Therefore, the empirical crater size-yield equation provides us a general and simple tool to estimate the yield for the explosions on the ground surface, although it ignored many important issues, for example, the range of yield used to create the equation is considerably smaller than the targeted events; many important parameters such as the material properties are not included in the equation; and additional nonlinear effects.

To test if it is applicable to other explosions, we further compared the yield estimation and waveforms of the Beirut explosion with two other open-pit explosions, the Xiangshui explosion on 21 March 2019, in east China (Song *et al.*, 2021) and the Tianjin explosion on 12 August 2015, in north China (Zhao, Feng, *et al.*, 2016). The *Lg* wave magnitudes for the Beirut, Xiangshui, and Tianjin explosions were $m_b(Lg)3.30 \pm 0.46$, 3.39 ± 0.24, and 2.87 ± 0.18, respectively. Figure 4a illustrates regional seismograms for these three explosions around an epicentral distance of 290 km. The Xiangshui explosion was caused by 600 tons of nitration waste which was equivalent to 260 tons of TNT according to the accident investigation report (see Data and Resources). The explosive that caused the Tianjin explosion was complex and reported to be equivalent to 430 tons of TNT according to the accident investigation report (see Data and Resources). Figure 4b illustrates the satellite photos of craters generated by the Beirut, Xiangshui, and Tianjin explosions, with their diameters of 100, 120, and 97 m, respectively. The heights of the burst were assumed to be 0.2 ~ 3.0 m for the Beirut explosion, 0.1 ~ 1.0 m for the Xiangshui explosion, and 0.5 ~ 2.0 m for the Tianjin explosion (for the Xiangshui and Tianjin explosions, the numbers are based on the official accident investigation reports by the accident investigation group of the State Council). Based on the above assumptions and equation (1), the yields estimated for the Beirut, Xiangshui, and Tianjin explosions were 0.48 ~ 2.30 kt, 0.49 ~ 1.88 kt, and 0.75 ~ 1.69 kt,

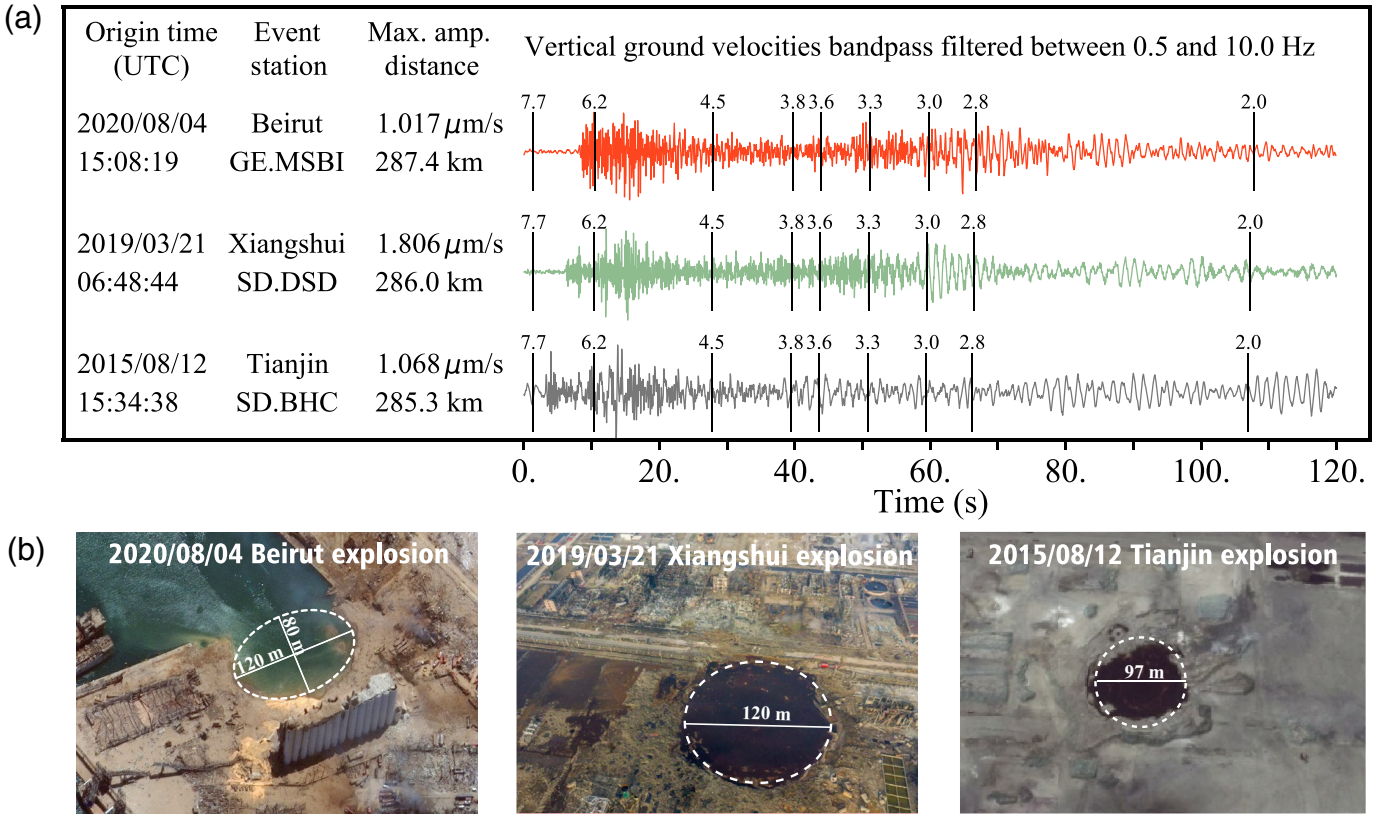

Figure 4. Comparison between the open-pit explosions of Tianjin, Xiangshui, and Beirut. (a) Normalized vertical component velocity waveforms bandpass filtered between 0.5 and 10.0 Hz for the Beirut (red), Xiangshui (light green), and Tianjin (light blue) explosions. Marked on the waveforms are apparent group velocities. (b) The satellite images of craters generated by the Beirut, Xiangshui, and Tianjin explosions (from google earth). The color version of this figure is available only in the electronic edition.

respectively, close to the reported yield. By comparing these estimated yields with their *Lg* wave magnitudes, the efficiency of converting the explosive energy into seismic energy for the Xiangshui explosion was higher than the other two explosions. The variation of the seismic efficiency has two possible causes: the uncertainty in estimating the height of burst and the difference in medium properties at source regions which the empirical equation (1) ignored. The Tianjin and Beirut explosions were both at port storage areas near the coast and likely with soft sediments, whereas the Xiangshui explosion is 40 km from the coastline and possibly with a harder ground. It is expected that the empirical equation may take its current form but its coefficients may change with different source parameters. Therefore, with the accumulation of data from broad yield ranges and source types, these coefficients can be calibrated.

Event Discrimination

The discrimination between explosions and natural earthquakes depends on the *P*- and *S*-wave contents they radiated (as illustrated in Fig. 3). The seismic *P/S* spectral ratios can reduce the propagation effect while highlighting the difference in source processes, providing an effective discriminant (Taylor *et al.*, 1989; Kim *et al.*, 1993; Walter *et al.*, 1995; Xie, 2002; Fisk, 2007; Richards and Kim, 2007; Allmann *et al.*, 2008; Pyle and Walter, 2019). We selected four nearby natural earthquakes and compared their spectral ratios with the Beirut explosion. We sampled *Pn*, *Pg*, *Sn*, and *Lg* waveforms from vertical-component regional seismograms through pure continental paths and calculated their Fourier spectra. After correcting the epicenter distances to a reference distance of 500 km and eliminating data with SNRs below 1.8, we calculated the *Pg/Lg*, *Pn/Lg*, and *Pn/Sn* spectral ratios at individual stations, followed by taking their

TABLE 2
Yield Estimations of the Beirut Explosion from Different Studies

Yield Estimation (kt)	Lower Limit (kt)	Upper Limit (kt)	References
0.5	–	1.12	Rigby *et al.* (2020)
1.0	0.91	1.09	Jorge (2021)
1.1	0.3	2.0	Pilger *et al.* (2021)
1.22	0.48	2.30	This study

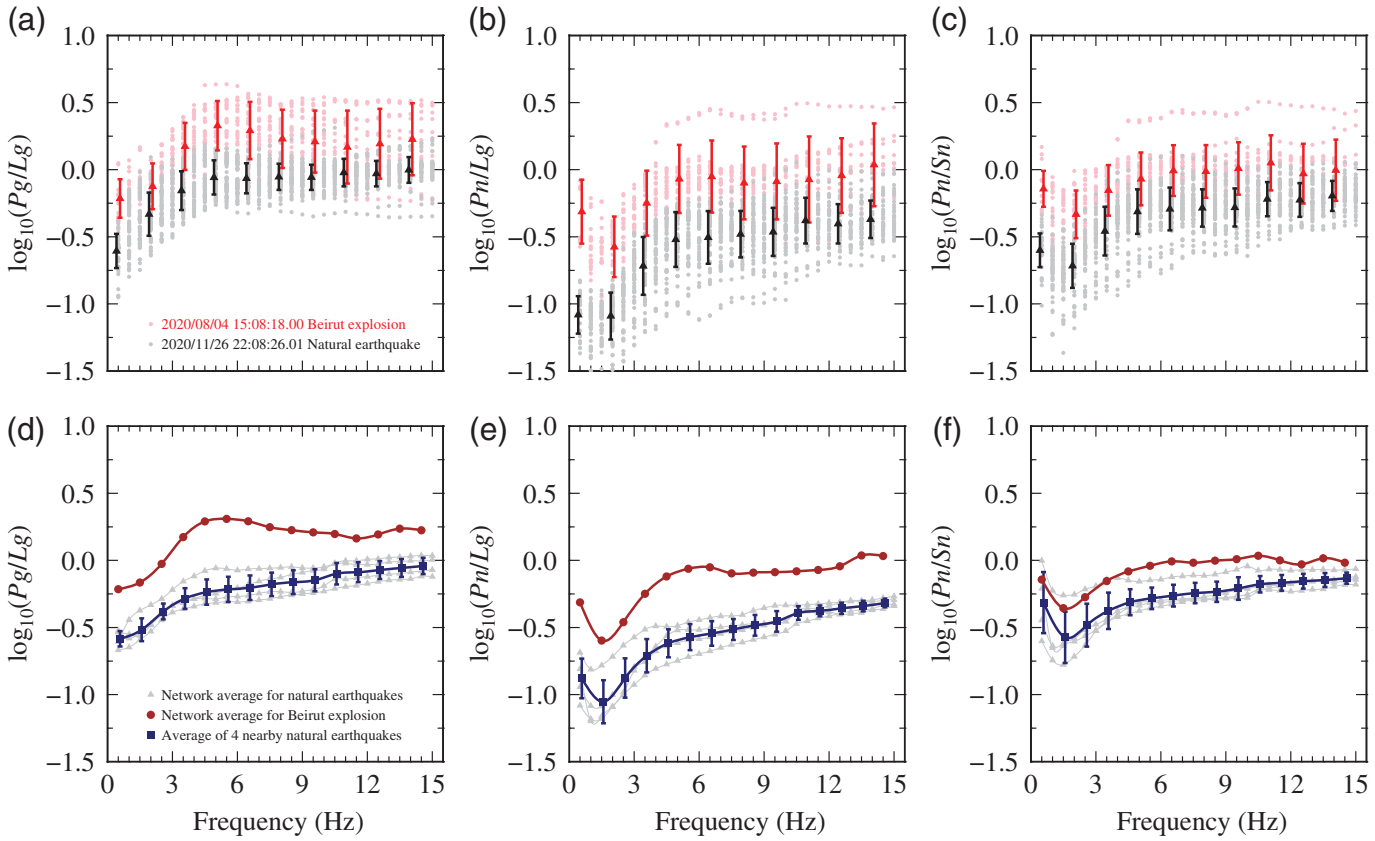

Figure 5. Spectral ratios *Pg/Lg*, *Pn/Lg*, and *Pn/Sn*. (a–c) Comparisons between the Beirut explosion (red) and a nearby earthquake (black). Light symbols indicate measurements from individual stations. Dark symbols are network-averaged values and their standard deviations. (d–f) Network-averaged ratios for the Beirut explosion (brown circles) and four natural earthquakes (gray triangle). The navy blue squares indicate the average of four natural earthquakes.

network averages. Figure 5a–c compare the *Pg/Lg*, *Pn/Lg*, and *Pn/Sn* spectral ratios for the Beirut explosion and a natural earthquake that occurred on 26 November 2020. The gray and pink dots are measurements from individual stations and dark-colored symbols are network-averaged values and their standard deviations. The network-averaged values reduced the scatter of the raw station results, greatly improved the reliability, and effectively expanded the available frequency band for discrimination. To further obtain typical spectral ratios for natural earthquakes, we averaged the spectral ratios of four natural earthquakes to create reference curves for discrimination (Fig. 5d–f). The results show that the Beirut explosion can be isolated from the earthquake populations by network-measured *Pg/Lg*, *Pn/Lg*, and *Pn/Sn* spectral ratios above 2.0 Hz.

In addition, we investigated the characteristics of spectral ratios of three open-pit explosions, the Beirut, Xiangshui, and Tianjin, and compared them with other types of sources including (1) 11 small chemical explosions, which were all 3-ton chemical explosions for reflection seismic survey purposes in Xinjiang, northwest China (Ma *et al.*, 2021) and detonated in wells in the hard rock at over buried depth, (2) six north Korean underground nuclear explosions, and (3) 20 earthquakes in selected regions including four near the Beirut explosion, four near the Xiangshui explosion, four near the Tianjin explosion, four in northwest China, and four in northeast China, respectively (Zhao, Feng, *et al.*, 2016; Zhao, Xie, *et al.*, 2016; He *et al.*, 2018; Ma *et al.*, 2021; Song *et al.*, 2021). Figure S1 shows the locations of these events and stations. The 11 small chemical explosions have uniform and simple source spectra with relatively high corner frequencies. To highlight variations between different source types, ratios of each type of source were averaged and then normalized by the average spectral ratio of 11 small explosions.

The results are shown in Figure 6a–c. Below 3 Hz, the spectral ratios show relatively complex features. Above which, we see a clear trend between different types of sources. As expected, nuclear explosions have the highest spectral ratios for their isotropic property, and natural earthquakes have the lowest spectral ratios for their dislocation mechanism. All chemical explosions are in between. The 11 small chemical explosions, although over buried, show relatively low spectral ratios, implying they generated considerable *S* energy. This could result from several reasons. For each of these shots, the explosives were charged in multiple wells in columns with

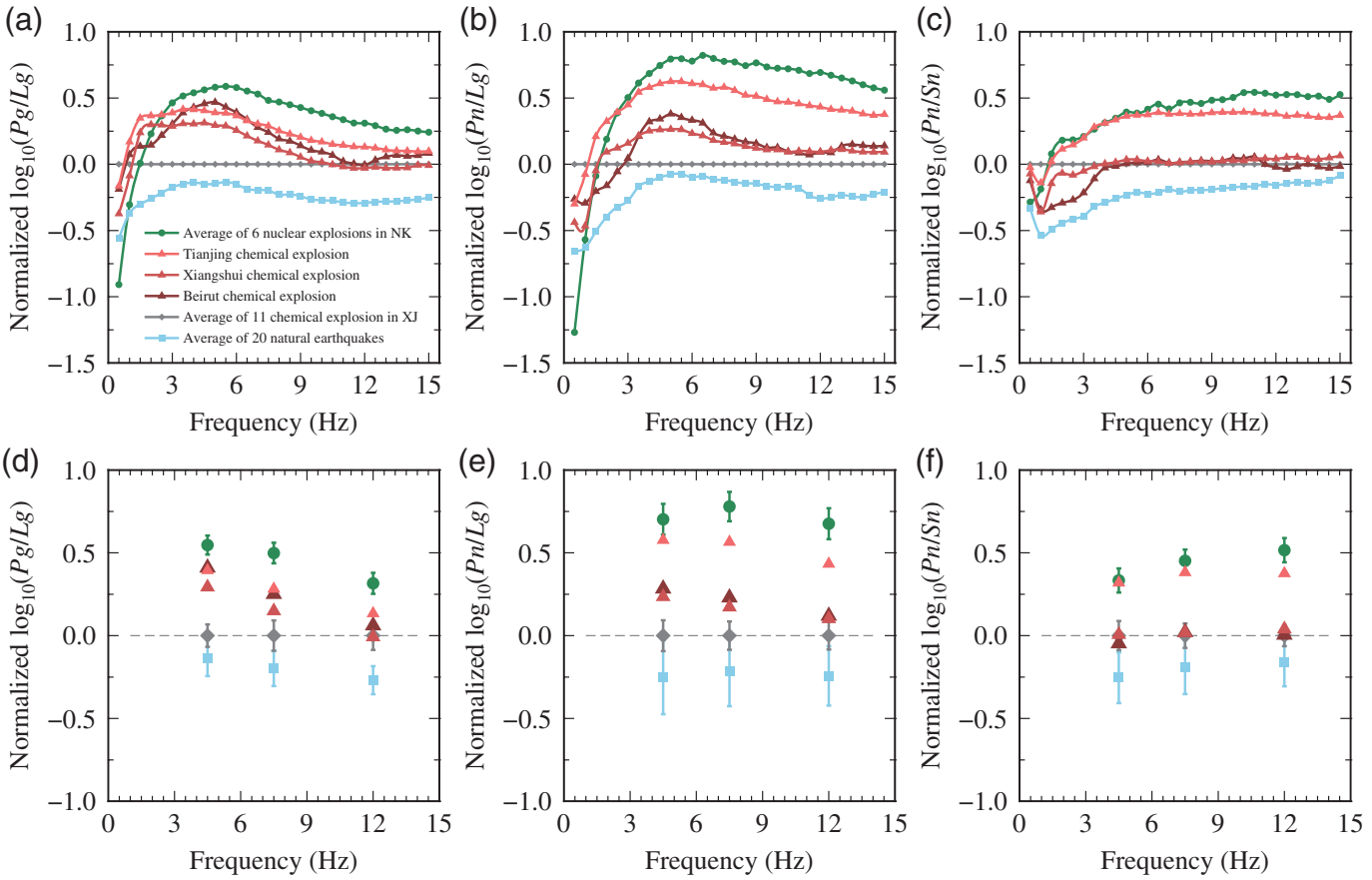

Figure 6. Comparisons of spectral ratios among different types of sources. All ratios are normalized by the average of 11 small underground explosions in Xinjiang. (a–c) Spectral ratios *Pg/Lg*, *Pn/Lg*, and *Pn/Sn* of three open-pit chemical explosions (Beirut, Xiangshui, and Tianjin) compared to the average of six underground nuclear explosions in north Korea (NK, green, He *et al.*, 2018), the average of 20 natural earthquakes (blue) near Beirut, Xiangshui, Tianjin, Xinjiang (XJ) and NK, and the average of 11 small underground chemical explosions in Xinjiang (gray, Ma *et al.*, 2021). (d–f) The earlier spectral ratios were further averaged within three frequency windows, 3–6, 6–9, and 9–15 Hz. The symbols are the same as panels (a–c). Note, the dashed rectangles indicate the ranges of three open-pit explosions.

their centroid located at 60 m deep, rather than spherically symmetric. These sources, although over buried (deeper than the scaled depth), were still very shallow. The low near-surface *P*-velocity made the radiated *P* wave can be trapped in the crust and converted into *Lg* waves (Xie and Lay, 1994). The *Rg* wave generated by a shallow source can be easily converted into *Lg* waves due to the scattering by near-surface lateral heterogeneities. Therefore, these small shallow chemical explosions tended to have lower *P/S* ratios than deeper nuclear explosions which were nearly perfectly spherically symmetric. Similar phenomena were also observed in northeast China by Richards and Kim (2007) and He *et al.* (2018); in northwest China by Ma *et al.* (2021); and east China by Song *et al.* (2021).

For moderate to large open-pit-explosions, their spectral ratios are generally higher than those from small shallow explosions but lower than those of nuclear explosions. In Figure 6a–c, for Beirut and Xiangshui explosions, all three ratios *Pg/Lg*, *Pn/Lg*, and *Pn/Sn* are very similar. However, for the Tianjin explosion, the *Pg/Lg* ratio is similar to the other two events, but its *Pn/Lg* and *Pn/Sn* ratios are considerably higher, approaching those of nuclear explosions. By investigating Figure 4a, we see the *Pn* wave from the Tianjin explosion is both faster and more prominent than from the other two explosions, likely the direct reason causing higher *Pn/Lg* and *Pn/Sn* ratios. The *Pn*-wave amplitude is very sensitive to the uppermost mantle velocity structure. A positive velocity gradient below the Moho discontinuity can both increase the *Pn* propagation velocity and its amplitude (Zhao *et al.*, 2015; Xie and Lay, 2016). On the other hand, for shallow sources, the *Pg* and *Lg* waves are mainly radiated horizontally but the *Pn* wave is more downward (Yang *et al.*, 2021). An open-pit explosion can be idealized into a vertical concentrated force applied on the ground surface, which naturally generates more *SV*-type waves than an isotropic explosion. Because the three open-pit explosions were all accidents and not tuned for specific engineering purposes, their radiation patterns may be complicated by the properties of chemical materials, their distributions, and detonation behaviors.

Figure 6d–f summarizes the earlier spectral features by further averaging these spectral ratios within the 3–6, 6–9, and 9–15 Hz frequency bands. The dashed rectangles specify the variation ranges of three open-pit explosions. These results reveal that the network-averaged spectral ratios show clear trends not only between explosions and natural earthquakes but also between different types of explosions. As accidental open-pit explosions, some of their *P/S* spectral ratios may close to nuclear explosions. Small chemical explosions for deep sounding or reflection purposes are widely available. Using spectral ratios of small explosions near the targeted regions to normalize the spectra may improve the accuracy of the spectral ratio method as a discriminant.

Discussions and Conclusions

Based on 221 broadband regional seismic records from 76 digital stations distributed in Cyprus Island, Mediterranean Sea bottom, Anatolia plateau, and northwestern Arabian plate, we investigated seismic characteristics of the Beirut explosion and four nearby earthquakes including the *Lg*-wave magnitude, the yield estimation, and event discrimination. The obtained magnitude for the Beirut explosion is $m_b(Lg) = 3.30 \pm 0.46$.

For yield estimation, the empirical magnitude-yield relation for buried explosions (Bowers *et al.* (2001) produced a yield of 0.112 kt, which greatly underestimated the yield of the Beirut explosion. Alternatively, based on the empirical relation by Ambrosini *et al.* (2002) and using the observed size of the crater and the assumed height of the burst, we obtained the yield for the Beirut explosion to be 1.22 kt, which is consistent with the number of explosives stored at the ground zero and similar to estimations based on other methods (Rigby *et al.*, 2020; Jorge, 2021; Pilger *et al.*, 2021). Through the earlier comparison, we conclude that, for an open-pit event such as the Beirut explosion, the energy conversion rate from the explosive charge to the seismic energy is considerably lower compared to that for a similar-size explosion if detonated fully buried in a hard rock condition. We further compared the magnitude and yield of the Beirut explosion with the other two open-pit chemical explosions in Xiangshui, China, and Tianjin port, China. The results showed that the Xiangshui explosion has higher seismic efficiency than the Tianjin and Beirut explosion, probably because the Tianjin and Beirut explosion occurred at port areas which are likely characterized by soft unconsolidated sediments, whereas the Xiangshui explosions occurred 40 km away from the coastline where the ground may be harder.

The crater size-yield empirical equation is obtained by Ambrosini *et al.* (2002) using a series of small charges. Many important factors which can affect the result are not properly included in the equation, for example, the range of yield used to create the equation is orders of magnitude smaller than the targeted events; parameters such as the material strength, water saturation, nonlinear property of the soil, are not considered. Fortunately, for these three large open-pit explosions, we have the number of explosives from independent sources. These numbers, although rough, permit us to compare the predicted yields with the actual yields and use the results to validate the empirical equation. Even though the applicability of the crater size-yield empirical equation should be further checked by more data, and possibly its coefficients be calibrated using observations from different regions and source conditions.

The regional *P/S* spectral ratios, including *Pg/Lg*, *Pn/Lg*, and *Pn/Sn*, were calculated for the Beirut explosion and four nearby natural earthquakes. These spectral ratios are effective in discriminating the open-pit explosion from the earthquake population. By further comparing the spectral ratios from different types of explosions including open-pit explosions, small buried chemical explosions, and historical nuclear explosions, the network-averaged *P/S* spectral ratios revealed certain differences among different types of explosions. Although these phenomena are based on limited samples investigated in this study, it appears *P/S* spectral ratios may tell us more information on the source and are worth further investigation.

Data and Resources

The waveforms used in this study are collected from the Incorporated Research Institutions for Seismology Data Management Center (IRIS-DMC) at https://ds.iris.edu/wilber3/find_event (last accessed December 2021) and German Research Center for Geosciences (GFZ) seismological data center GEOFOrschungsNetz (GEOFON) at https://geofon.gfz-potsdam.de (last accessed December 2021). Certain figures were generated using Generic Mapping Tools (GMT, Wessel *et al.*, 2019). The Report on the 21 March Explosion Accident in Xiangshui, Jiangsu Province, by the accident investigation group of the State Council, available at http://www.zjpy.gov.cn/art/2019/11/27/art_1440029_40543658.html (last accessed February 2022). Investigation report on the 12 August Fire and Explosion Accident in Tianjin Port, by the accident investigation group of the State Council, available at http://www.gov.cn/foot/2016-02/05/5039788/files/460731d8cb4c4488be3bb0c218f8b527.pdf (last accessed February 2022). The supplemental material article includes two figures and one table. Figure S1 shows the locations of events and stations used in the investigation for the characteristics of spectral ratios of different sources. Figure S2 shows an online photo of the warehouse before the explosion in Beirut port which testifies to our estimation of the burst height for the Beirut explosion. Table S1 lists the station parameters used in the Beirut explosion investigation.

Declaration of Competing Interests

The authors acknowledge that there are no conflicts of interest recorded.

Acknowledgments

Editor in Chief A. Bent, an anonymous reviewer, and reviewer M. E. Pasyanos are appreciated for valuable comments that greatly improved this article. This research was supported by the National Natural Science Foundation of China (Grant Numbers 41974061, 41974054, U2139206, and 42104055) and the National Key Research and Development Program of China (Grant Number 2017YFC0601206).

References

Allmann, B. P., P. M. Shearer, and E. Hauksson (2008). Spectral discrimination between quarry blasts and earthquakes in southern California, *Bull. Seismol. Soc. Am.* **98,** 2073–2079.

Ambraseys, N. N. (1990). Uniform magnitude re-evaluation of European earthquakes associated with strong-motion records, *Earthq. Eng. Struct. Dynam.* **19,** 1–20.

Ambrosini, R. D., B. M. Luccioni, R. F. Danesi, J. D. Riera, and M. M. Rocha (2002). Size of craters produced by explosive charges on or above the ground surface, *Shock Waves* **12,** 69–78.

Bennett, T. J., and J. R. Murphy (1986). Analysis of seismic discrimination capabilities using regional data from western United States events, *Bull. Seismol. Soc. Am.* **76,** 1069–1086.

Bonner, J., R. B. Herrmann, D. Harkrider, and M. Pasyanos (2008). The surface wave magnitude for the 9 October 2006 north Korean nuclear explosion, *Bull. Seismol. Soc. Am.* **98,** 2498–2506.

Bowers, D., P. D. Marshall, and A. Douglas (2001). The level of deterrence provided by data from the SPITS seismometer array to possible violations of the Comprehensive Test Ban in the Novaya Zemlya region, *Geophys. J. Int.* **146,** 425–438.

Buehler, J. S., and P.M. Shearer (2015). T phase observations in global seismogram stacks, *Geophys. Res. Lett.* **42,** 6607–6613.

Chun, K. Y., Y. Wu, and G. A. Henderson (2011). Magnitude estimation and source discrimination: A close look at the 2006 and 2009 north Korean underground nuclear explosions, *Bull. Seismol. Soc. Am.* **101,** 1315–1329.

Fisk, M. (2007). Source spectral modeling of regional P/S discriminants at nuclear test sites in China and the Former Soviet Union, *Bull. Seismol. Soc. Am.* **96,** 2348–2367.

Fisk, M., D. Jepsen, and J. R. Murphy (2002). Experimental seismic event-screening criteria at the Prototype International Data Center, *Pure Appl. Geophys.* **159,** 865–888.

Ghalib, H. A. A., G. Kraft, A. Alchalbi, and R. Wagner (2021). Seismic location of the 4 August 2020 Beirut port chemical explosion, *Seismol. Res. Lett.* **93,** 33–44.

Gibbons, S. J., F. Pabian, S. P. Näsholm, T. Kværna, and S. Mykkeltveit (2017). Accurate relative location estimates for the north Korean nuclear tests using empirical slowness corrections, *Geophys. J. Int.* **208,** 101–117.

Guglielmi, G. (2020). Why Beirut's ammonium nitrate blast was so devastating, *Nature* doi: 10.1038/d41586-020-02361-x.

He, X., L. F. Zhao, X. B. Xie, X. Tian, and Z. X. Yao (2021). Weak crust in southeast Tibetan plateau revealed by Lg-wave attenuation tomography: Implications for crustal material escape, *J. Geophys. Res.* **126,** 1–17.

He, X., L. F. Zhao, Z. X. Yao, and X. B. Xie (2018). High-precision relocation and event discrimination for the 3 September 2017 underground nuclear explosion and subsequent seismic events at the north Korean test site, *Seismol. Res. Lett.* **89,** 2042–2048.

Jorge, S. D. (2021). Explosion analysis from images: Trinity and Beirut, *Eur. J. Phys.* **42,** no. 3, 035803, doi: 10.1088/1361-6404/abe131.

Kim, W. Y., and P. G. Richards (2007). North Korean nuclear test: Seismic discrimination at low yield, *Eos Trans. AGU* **88,** 158–161.

Kim, W.-Y., D. W. Simpson, and P. G. Richards (1993). Discrimination of earthquakes and explosions in the eastern United States using regional high-frequency data, *Geophys. Res. Lett.* **20,** 1507–1510.

Koper, K. D., M. M. Holt, J. R. Voyles, R. Burlacu, M. L. Pyle, R. Wang, and B. Schmandt (2020). Discrimination of small earthquakes and buried single-fired chemical explosions at local distances (<150 km) in the western United States from comparison of local magnitude (ML) and coda duration magnitude (MC), *Bull. Seismol. Soc. Am.* **111,** 558–570.

Koyanagi, S., K. Aki, N. Biswas, and K. Mayeda (1995). Inferred attenuation from site effect-corrected T phases recorded on the island of Hawaii, *Pure Appl. Geophys.* **144,** 1–17.

Laske, G., G. Masters, Z. Ma, and M. Pasyanos (2013). Update on CRUST1.0—A 1-degree Global Model of Earth's Crust, *EGU General Assembly 2013*, Vienna, Austria.

Ma, X., L. F. Zhao, X. B. Xie, X. He, and Z. X. Yao (2021). Regional seismic characteristics of chemical explosions on the eastern margin of the Junggar basin, northwest China, and of historical Semipalatinsk nuclear tests, *Bull. Seismol. Soc. Am.* **111,** 606–620.

Murphy, J. R., J. L. Stevens, B. C. Kohl, and T. J. Bennett (2013). Advanced seismic analyses of the source characteristics of the 2006 and 2009 north Korean nuclear tests, *Bull. Seismol. Soc. Am.* **103,** 1640–1661.

Myers, S. C., S. R. Ford, R. J. Mellors, S. Baker, and G. Ichinose (2018). Absolute locations of the north Korean nuclear tests based on differential seismic arrival times and InSAR, *Seismol. Res. Lett.* **89,** 2049–2058.

Nemer, T. S. (2021). The Beirut port explosion: A geoscience perspective, *Seismol. Res. Lett.* **92,** 2093–2098.

Nuttli, O. W. (1973). Seismic wave attenuation and magnitude relations for eastern North America, *J. Geophys. Res.* **78,** 876–885.

Nuttli, O. W. (1986a). Lg magnitudes of selected east Kazakhstan underground explosions, *Bull. Seismol. Soc. Am.* **76,** 1241–1251.

Nuttli, O. W. (1986b). Yield estimates of Nevada test site explosions obtained from seismic Lg waves, *J. Geophys. Res.* **91,** 2137–2151.

Pasyanos, M. E., and S. C. Myers (2018). The coupled location/depth/yield problem for north Korea's declared nuclear tests, *Seismol. Res. Lett.* **89,** 2059–2067.

Patton, H. J., and J. Schlittenhardt (2005). A transportable mb(Lg) scale for central Europe and implications for low-magnitude Ms–mb discrimination, *Geophys. J. Int.* **163,** 126–140.

Pilger, C., P. Gaebler, P. Hupe, A. C. Kalia, F. M. Schneider, A. Steinberg, H. Sudhaus, and L. Ceranna (2021). Yield estimation of the 2020 Beirut explosion using open access waveform and remote sensing data, *Sci. Rep.* **11,** doi: 10.1038/s41598-021-93690-y.

Pyle, M. L., and W. R. Walter (2019). Investigating the effectiveness of P/S amplitude ratios for local distance event discrimination, *Bull. Seismol. Soc. Am.* **109,** 1071–1081.

Richards, P., and W.-Y. Kim (2007). Seismic signature, *Nat. Phys.* **3,** 4–6.

Rigby, S. E., T. J. Lodge, S. Alotaibi, A. D. Barr, S. D. Clarke, G. S. Langdon, and A. Tyas (2020). Preliminary yield estimation of the 2020 Beirut explosion using video footage from social media, *Shock Waves* **30,** 671–675.

Ringdal, F., P. D. Marshall, and R. W. Alewine (1992). Seismic yield determination of Soviet underground nuclear explosions at the Shagan river test site, *Geophys. J. Int.* **109,** 65–77.

Schaff, D. P., W. Y. Kim, P. G. Richards, E. Jo, and Y. Ryoo (2018). Using waveform cross correlation for detection, location, and identification of aftershocks of the 2017 nuclear explosion at the north Korea test site, *Seismol. Res. Lett.* **89,** 2113–2119.

Selby, N. D., P. D. Marshall, and D. Bowers (2012). mb:Ms event screening revisited, *Bull. Seismol. Soc. Am.* **102,** 88–97.

Shin, J. S., D.-H. Sheen, and G. Kim (2010). Regional observations of the second north Korean nuclear test on 2009 May 25, *Geophys. J. Int.* **180,** 243–250.

Song, Y., L.-F. Zhao, X.-B. Xie, X. Ma, G. Du, X. Tian, and Z.-X. Yao (2021). Seismological observations on the 2019 March 21 accidental explosion at Xiangshui chemical plant in Jiangsu, China, *Geophys. J. Int.* **228,** 538–550.

Stevens, J. L., and S. M. Day (1985). The physical basis of mb: Ms and variable frequency magnitude methods for earthquake/explosion discrimination, *J. Geophys. Res.* **90,** no. B4, 3009–3020.

Talandier, J., and E. A. Okal (1998). On the mechanism of conversion of seismic waves to and from T waves in the vicinity of island shores, *Bull. Seismol. Soc. Am.* **88,** 621–632.

Taylor, S. R., M. D. Denny, E. S. Vergino, and R. E. Glaser (1989). Regional discrimination between NTS explosions and western U.S. earthquakes, *Bull. Seismol. Soc. Am.* **79,** 1142–1176.

Wagner, M., S. Husen, A. Lomax, E. Kissling, and D. Giardini (2013). High-precision earthquake locations in Switzerland using regional secondary arrivals in a 3-D velocity model, *Geophys. J. Int.* **193,** 1589–1607.

Walter, W., K. Mayeda, and H. Patton (1995). Phase and spectral ratio discrimination between NTS earthquakes and explosions. Part I: Empirical observations, *Bull. Seismol. Soc. Am.* **85,** 1050–1067.

Walter, W. R., D. A. Dodge, G. Ichinose, S. C. Myers, and S. R. Ford (2018). Body wave methods of distinguishing between explosions, collapses, and earthquakes: Application to recent events in north Korea, *Seismol. Res. Lett.* **89,** 2131–2138.

Walter, W. R., E. Matzel, M. E. Pasyanos, D. B. Harris, R. Gok, and S. R. Ford (2007). Empirical observations of earthquake-explosion discrimination using P/S ratios and implications for the sources of explosion S-waves, *29th Monitoring Research Review: Ground-Based Nuclear Explosion Monitoring Technologies*, 684–693.

Wessel, P., J. F. Luis, L. Uieda, R. Scharroo, F. Wobbe, W. H. F. Smith, and D. Tian (2019). The generic mapping tools version 6, *Geochem. Geophys. Geosys.* **20,** 5556–5564.

Xie, J. (2002). Source scaling of Pn and Lg spectra and their ratios from explosions in central Asia: Implications for the identification of small seismic events at regional distances, *J. Geophys. Res.* **107,** no. 7, doi: 10.1029/2001JB000509.

Xie, X. B., and T. Lay (1994). The excitation of Lg waves by explosions: A finite-difference investigation, *Bull. Seismol. Soc. Am.* **84,** 324–342.

Xie, X. B., and T. Lay (2016). Effects of laterally varying mantle lid velocity gradient and crustal thickness on Pn geometric spreading with application to the north Korean test site, *Bull. Seismol. Soc. Am.* **107,** 22–33.

Yang, G., L. F. Zhao, X. B. Xie, L. Zhang, and Z. X. Yao (2021). High-precision relocation with the burial depths of the north Korean underground nuclear explosions by combining Pn and Pg differential traveltimes, *J. Geophys. Res.* **126,** e2020JB020745.

Zhang, M., and L. Wen (2013). High-precision location and yield of north Korea's 2013 nuclear test, *Geophys. Res. Lett.* **40,** 2941–2946.

Zhang, T.-R., and T. Lay (1995). Why the Lg phase does not traverse oceanic crust, *Bull. Seismol. Soc. Am.* **85,** 1665–1678.

Zhao, L. F., and X. B. Xie (2016). Strong Lg-wave attenuation in the middle east continental collision orogenic belt, *Tectonophysics* **674,** 135–146.

Zhao, L. F., X. B. Xie, B. F. Tian, Q. F. Chen, T. Y. Hao, and Z. X. Yao (2015). Pn wave geometrical spreading and attenuation in northeast China and the Korean peninsula constrained by observations from north Korean nuclear explosions, *J. Geophys. Res.* **120,** 7558–7571.

Zhao, L. F., X. B. Xie, W. M. Wang, N. Fan, X. Zhao, and Z. X. Yao (2017). The 9 September 2016 north Korean underground nuclear test, *Bull. Seismol. Soc. Am.* **107,** 3044–3051.

Zhao, L. F., X. B. Xie, W. M. Wang, J. L. Hao, and Z. X. Yao (2016). Seismological investigation of the 2016 January 6 north Korean underground nuclear test, *Geophys. J. Int.* **206,** 1487–1491.

Zhao, L. F., X. B. Xie, W. M. Wang, and Z. X. Yao (2008). Regional seismic characteristics of the 9 October 2006 north Korean nuclear test, *Bull. Seismol. Soc. Am.* **98,** 2571–2589.

Zhao, L. F., X. B. Xie, W. M. Wang, and Z. X. Yao (2012). Yield estimation of the 25 May 2009 north Korean nuclear explosion, *Bull. Seismol. Soc. Am.* **102,** 467–478.

Zhao, X., W. Feng, Y. Tan, J. Li, S. Pei, Y. An, W. Hua, S. He, Y. Zhao, J. Liu, and Z. Yao (2016). Seismological investigations of two massive explosions in Tianjin, China, *Seismol. Res. Lett.* **87,** 826–836.

Manuscript received 22 December 2021
Published online 25 May 2022